A framework for multiplex imaging optimization and reproducible analysis

Jennifer Eng[1,2], Elmar Bucher[1], Zhi Hu[1], Ting Zheng [3], Summer L. Gibbs[1,2], Koei Chin[1,2*] and Joe W. Gray[1,2]*

[1]Department of Biomedical Engineering, School of Medicine, Oregon Health and Science University, Portland, OR 97239 USA.

[2]Knight Cancer Institute, School of Medicine, Oregon Health and Science University, Portland, OR 97239 USA.

[3]Cancer Early Detection Advanced Research Center, School of Medicine, Oregon Health and Science University, Portland, OR 97239 USA.

[*]To whom all correspondence should be addressed:

Joe W. Gray, Oregon Health and Science University, Robertson Life Sciences Building, 2730 S Moody Ave, Mail Code: CL3G, Portland, OR 97201. Email: grayjo@ohsu.edu, Phone: 503-494-3021

Koei Chin, Oregon Health and Science University, Robertson Life Sciences Building, 2730 S Moody Ave, Mail Code: CL3G, Portland, OR 97201. Email: KoeiChin@ohsu.edu, Phone: 503-494-0519

Abstract

Multiplex imaging technologies are increasingly used for single-cell phenotyping and spatial characterization of tissues; however, transparent methods are needed for comparing the performance of platforms, protocols and analytical pipelines. We developed a python software, mplexable, for reproducible image processing and utilize Jupyter notebooks to share our optimization of signal removal, antibody specificity, background correction and batch normalization of the multiplex imaging with a focus on cyclic immunofluorescence (CyCIF). Our work both improves the CyCIF methodology and provides a framework for multiplexed image analytics that can be easily shared and reproduced.

Introduction

Multiplex imaging methods enable quantification of numerous proteins in tissues while retaining spatial and morphological information. In many contexts, dozens of targets must be labeled in an intact tissue section to identify key cell types and quantify their spatial relationships. Multiplex imaging technologies utilize various strategies to overcome the limitation of conventional immunofluorescence (IF) protocols that label a few markers per section. Five and seven-plex immunohistochemistry (IHC) has been achieved by fluorophore-conjugated tyramide deposited on the tissue[1–3]. Twelve to 29-plex immunohistochemistry (IHC) is enabled with alcohol-soluble peroxidase substrate 3-amino-9-ethylcarbazole (AEC) detection combined with antibody stripping[4,5] and 40-plex IF can be achieved with antibody elution in iterative indirect immunofluorescence imaging (4i)[6] and multiple interactive labeling by antibody neodeposition (MILAN)[7,8]. Direct immunofluorescence using fluorophore-conjugated primary antibodies and chemical inactivation of fluorescent dyes enables detection of over 50 protein targets in a single tissue section, in cyclic immunofluorescence (CyCIF)[9–11], NeoGenomics' MultiOmyx platform[12], and iterative bleaching extends multiplexity (IBEX)[13]. Similarly, multi-epitope-ligand cartography (MELC), employs photo-inactivation of fluorescently labeled antibodies[14,15].

Furthermore, fluorophore-conjugated DNA barcodes (i.e., oligonucleotides) facilitate multiplexing in co-detection by indexing (Akoya's CODEX)[16], Ultivue's InSituPlex[17], Immuo-SABER[18], and Ab-oligo cyCIF[19]. Imaging mass cytometry[20] and multiplex ion beam imaging[21] can detect over 40 antibodies conjugated to metal reporters by time-of-flight mass-spectrometry. The Nanostring GeoMx[22] platform can detect >100 protein targets conjugated to oligonucleotide barcodes, although the data are not images, but spatially registered counts of released oligos[23]. All of these methods rely on specific labeling of proteins with antibodies, a process that must be validated by studies that establish specificity, sensitivity and reproducibility. Ideally this is accomplished via transparent analyses using well documented, open-source image analysis pipelines.

Herein, we quantitatively assess antibody labeling in one multiplex imaging platform, CyCIF[9–11], while varying antibody application strategies, fluorescence signal and tissue autofluorescence removal methods, and experimental batches. This resulted in several strategies to improve CyCIF, including optimization of aspects of chemical bleaching, autofluorescence correction, antibody application order and batch normalization. Herein, we build on protocol optimization efforts[10,24] and share our image processing pipeline software, the free and open source python library, mplexable (Figure 1a-b). Finally, we introduce a framework for reproducible image analysis and visualization. Our analytics comprise linked and executable code and data that enabled all figures and analytical results in our paper to be fully reproduced from the accompanying image data (https://www.synapse.org/#!Synapse:syn23644107), processed data and code (https://github.com/engjen/cycIF_Validation). We used Jupyter notebooks to link code, data, metadata and the computational environment in a machine- and human-readable document (Figure 1c, Table 1). Although we focused on validation of a single platform, our tools for image analysis facilitate quantitative and reproducible characterization of tissues by any multiplex imaging platform.

Results and Discussion

Adopting the method of Lin *et al.*[9], we stained formalin-fixed, paraffin-embedded (FFPE) tissues using a cyclic process in which four proteins per cycle were labeled using a direct immunofluorescence (IF) protocol, imaged, and quenched of fluorescence signal (Figure 1a, dx.doi.org/10.17504/protocols.io.23vggn6). We typically labeled 40 – 60 proteins per slide before tissue and staining quality degraded (quantified in Figure 2e and Supplementary Figure 7, respectively). We developed free and open-source tools to perform quality control on images and metadata and automate image processing from registration through single-cell segmentation and feature extraction (Figure 1b, https://pypi.org/project/mplexable/). Finally, we shared all analytics used to produce figures and conclusions as linked and executable code and data (Figure 1c). Jupyter notebooks serve as a human and machine-readable record that described the data, image analysis steps and computational environment, both enabling replication of our findings and linking data and metadata to facilitate use by others.

Comparison to Standard IF

We benchmarked our CyCIF protocol against a direct IF protocol. CyCIF staining in normal and malignant breast tissue was compared to standard direct IF on adjacent tissue sections. Antibodies and staining conditions were selected that produced visually similar staining patterns in both CyCIF and standard IF staining (Figure 2a, Notebook 1-1, [NB1-1]). For quantification, we set an intensity threshold for each marker, with all pixels above the set threshold considered positive. All pixels at least 10 micrometers away from positive staining were considered background pixels (the 10 µm gap was to exclude any influence of lateral bleed through around positive pixels; Figure 2b, Supplementary Figure 1, NB2-1). If a marker was negative in a given tissue section, it was not analyzed in that tissue. Although the positive and background intensity varied between conditions, presumably due to the

imprecisions introduced by manual pipetting, the relative signal-to-background ratio (SBR, see methods) of standard IF compared to CyCIF was near one (relative SBR: mean=0.96, standard error of the mean [SEM]=0.22) and highly correlated (Pearson R=0.89, p=1.6e-9, Figure 2c, Supplementary Figure 1, NB2-2). We assessed specificity between conditions by segmenting single cells and counting positive cells with a mean intensity above the set threshold. We found that the percentage of positive cells of standard IF relative to CyCIF was also near one (relative % positive: mean=0.96, SEM=0.18) and the fraction positive was highly correlated (Pearson R=0.99, p=5.8e-24, Figure 2c, Supplementary Figure 1c, NB2-2). We concluded that the SBR and specificity of antibody staining in the first five cycles of CyCIF is similar to standard IF, the cyclic process does not excessively impact tissue staining, and CyCIF offers the advantage of detecting increased marker combinations while utilizing a single slide.

Tissue Loss Characterization

The CyCIF process resulted in increased tissue loss compared to standard IF (Supplementary Figure 1a, NB2-1). In order to characterize the numbers and types of cells and tissues that were susceptible to tissue loss during CyCIF, three adjacent sections of a 72-core tissue microarray (TMA) containing normal and malignant tissues were repeatedly quenched and imaged (Figure 2d). Slow but steady tissue loss was observed over 10 rounds of CyCIF, with 95% of cells remaining after 10 rounds (Figure 2e). We found that the 18 normal tissues suffered more tissue loss than the 52 malignant and 2 benign tissues (Figure 2e), and the difference in fraction of cells remaining after ten rounds was significant (Figure 2f). We found no difference in the number of cells lost in tissues separated by stage or grade, or by cells separated by their nuclear size and shape (which correlate with epithelial, immune, endothelial or mesenchymal cell types, Figure 2f, g, h). While all malignant tissues were obtained from autopsy, normal tissues obtained from surgical resections vs. autopsy showed a trend towards reduced tissue loss (Mann-Whitney U, p=0.083). This could reflect tissue processing variation, as smaller tissue size and

longer time in fixation have been shown to reduce section detachment in immunohistochemistry[25]. There were significant differences in tissue loss in normal tissues from different organs and malignant tissues with different pathologies (Supplementary Figure 3). Our results suggest that tissue loss varied more between different tissues than between individual cell types within a given tissue.

Quenching Condition Assessment

Most tissue loss was observed during the quenching step, necessitating development of gentle yet effective conditions for complete signal removal. CyCIF fluorescence signal removal was accomplished by chemical quenching of fluorescent dyes using hydrogen peroxide (H_2O_2). Only certain dyes, including Alexa Fluor (AF)-488, AF555, AF647 and AF750, were quenchable using this method. Other dyes, including AF546 and fluorescein, were resistant to quenching, as previously reported[24]. Increasing H_2O_2 concentration from 3% to 4.5% or 6% in 20 mM sodium hydroxide did not improve quenching rate, and additional time in H_2O_2 also failed to completely eliminate strong signal (Figure 3a, b, d Supplementary Figure 4, 5 NB3-1). Gentle heating with an incandescent light placed ~4 inches above the sample during quenching (see methods) appeared to increase the rate of H_2O_2 oxidation (estimated by heat generation, Supplementary Figure 5c), resulting in complete signal removal (Figure 3c, d Supplementary Figure 5 a, b, NB3-1). Quantification of the unstained negative controls in all quenching conditions showed that mean tissue autofluorescence decreased during the first quench (AF488: mean 22% decrease, SEM=2.8%; AF555: mean 24% decrease, SEM=2%, AF647: mean 5% decrease, SEM=1.4%, n=3), a decrease not seen in an unquenched tissue that was repeatedly imaged (Supplementary Figure 5e, f, NB3-1). Therefore, we standardized quenching using 3% H_2O_2 for 30 minutes with incandescent light and added an additional round of quenching (i.e., pre-quenching before CyCIF staining) similar to others[10], to reduce overall tissue autofluorescence by roughly 25% (Supplementary Figure 5e).

Antibody Order Evaluation and Improvement

Finally, we tested if the order of antibody application in the CyCIF panel influenced antibody sensitivity and specificity. We applied an 11-round, 44-antibody panel twice to the same TMA, for a total of 22 rounds (Supplementary Table 1). We visually and quantitatively compared the antibody staining pattern and single cell mean intensities of the images acquired after the first application of each antibody to the second (Supplementary Figure 6, NB3-3). Of the 44 antibodies evaluated, 86% had a high Pearson correlation (>0.8) between first and second applications, but 81% had lower dynamic range and SBR on the second application (Supplementary Figure 7, NB3-4). Effects of double-application were antibody and epitope specific, as 28% antibodies showed similar dynamic range (<50% change) on the second application, and 62% still had an estimated SBR>1.5 on the second application, versus 78% on the first (Supplementary Figure 7, NB3-4). Non-specific nuclear staining was observed for several antibodies conjugated to the AF750 fluorophore, and unexpectedly, it diminished on the second application (Supplementary Figure 6c, NB3-4). We tested several potential variables impacting stain quality in later rounds, including non-specific IgG interactions, non-specific fluorophore interactions, specific IgG interactions, and quenching effects. Out of all of these, the only condition that apparently reduced non-specific nuclear background was additional quenching (Supplementary Figure 8). Thus, we designed an improved panel order which positioned antibody-conjugates tending to have non-specific staining in a later round (Figure 3e), as well as addressed challenges of autofluorescence, channel bleed through and incomplete quenching (Figure 3f-j, Supplementary Table 2). We compared the original and optimized orders on near-adjacent slides cut from a TMA containing three tissues with positive staining for each marker. SBR quantification was completed by applying a threshold to each marker to find positive pixels, and manually selecting areas of non-specific background (e.g., tumor nests for immune markers and stromal areas for tumor markers). Our new panel order significantly increased SBR (Figure 3i, NB3-

5). In earlier rounds we prioritized antibodies to antigens with varied expression levels such as human epidermal growth factor receptor 2 (HER2), E-cadherin and cytokeratins, which generally lose their dynamic range in later staining rounds. We placed immune cell markers in later rounds, as they have a binary (i.e., on/off) expression pattern and sometimes showed better SBR in later rounds, due to decreased background (Figure 3e, f, j). Markers expressed in the same cell type and/or subcellular location were placed in non-adjacent channels and rounds to allow detection artifacts from channel bleed through and any incomplete quenching. Bleed through was evident for weakly staining and strongly staining antibodies in adjacent channels (e.g., PD1-AF647 and CK19-AF750, Figure 3 g, j), but was minimized by avoiding such combinations in the same round. Bleed through was not specific to our selected fluorophores and filter sets, as we observed FITC to PE bleed through in another multiplex imaging platform, which could also be mitigated by avoiding strongly staining and weakly staining antibodies in adjacent channels (Supplementary Figure 8, NB3-6).

Autofluorescence Dynamics and Corrections

Although pre-quenching reduced overall tissue autofluorescence by ~25% (Supplementary Figure 5 e), we sought to develop a method to computationally subtract remaining autofluorescence, which, in some tissue structures, was brighter than the biomarker staining. First, we characterized single-cell autofluorescence dynamics over rounds of CyCIF by quantifying single-cell AF488 intensity in three unstained normal pancreas tissues that had been imaged and quenched repeatedly. We segmented the nuclei based on DAPI staining and expanded each nucleus by five pixels to capture the cytoplasm. Tissues were batch normalized and unsupervised clustering revealed groups of cells with comparable autofluorescence profiles over the experiment that localized to similar regions in each tissue (Supplementary Figure 9, NB4-1). Overlaying the cells in each cluster on the tissue revealed cells in cluster seven comprised tissue structures with bright autofluorescence that covered a wide spectrum

from DAPI to AF488 channels (Figure 4a). Quantification of mean cluster intensity over rounds of quenching showed that while other clusters' intensities stayed constant, the cluster seven intensity dropped linearly between one and four rounds of quenching (Figure 4c, NB3-1, NB4-1). To confirm these results, we collected two additional datasets, three adjacent sections from a 72-core TMA containing normal and tumor tissues (Figure 4d) and three adjacent sections from an 11-core TMA containing HER2+ breast cancer tissues. The two groups of slides were quenched for a total of 10 rounds, 330 minutes and 6 rounds, 210 minutes, respectively. We segmented cells to obtain single-cell autofluorescence values, batch normalized and clustered as described for the pancreas tissue (Figure 4 e-g, Supplementary Figure 10). Although the AF488 autofluorescence initially declined in these datasets, as had been observed in the pancreas, surprisingly it increased in later rounds, globally across all clusters (Figure 4 h). We did observe that the autofluorescence clusters correlated with one or more tissue types and pathologies (Figure 4j, Supplementary Fig 11), but they all showed the same trend, with a minimum intensity at three or four rounds of quenching (after pre-quenching, Figure 4 h, Supplementary Figure 12). We saw similar trends in AF555 autofluorescence (Supplementary Figure 11, 12). Therefore, to computationally remove autofluorescence without over-subtracting, we recommend collecting baseline autofluorescence images after quenching at round three or four, and subtracting these, scaled by exposure time, from AF488, AF555 and AF647 channels. Subtraction from the AF750 channel appeared unnecessary, given its minimal autofluorescence. This procedure will remove an additional 60 – 70% of autofluorescence from the brightest rounds (Figure 4i, Supplementary Figure 11, 12). Since different tissues and other multiplex imaging platforms may exhibit different autofluorescence dynamics, we implemented both the baseline algorithm and a scaled algorithm, which assumes linear increase or decrease in autofluorescence, for autofluorescence subtraction in mplexable. We found that the scaled algorithm, by linearly interpolating autofluorescence between background images collected at the beginning and end of staining, did reduce false positives for some markers in our panel (Supplementary

Figure 11). Since the brightest areas of autofluorescence showed linear decrease across the first few rounds of CyCIF, the scaled algorithm was most advantageous in tissues with strong autofluorescence that are stained with only a few rounds of CyCIF. On the other hand, the baseline algorithm is simple, requiring collection of just one background image, and can remove the majority of autofluorescence background without over-subtraction in various tissue and experimental contexts.

Reproducibility and Batch Normalization

Following panel optimization, we assessed the reproducibility of CyCIF by analyses of three serial TMA sections stained with the same 20-antibody panel on different dates (Figure 5a). We used manual thresholding to quantify SBR, as in our standard versus CyCIF analysis (Supplementary Figure 13a, b, NB5-1). We compared our manual method of SBR calculation to the use of intensity quantiles to estimate dynamic range[10], and found that manual thresholds were more reliable when markers were negative, (e.g., HER2 in normal breast, Supplementary Figure 14, NB5-2). With both methods, we found that the ratio of SBR between replicates for all 20 antibodies was close to one (relative SBR: mean=1.02, SEM=0.23, n=20, Figure 5b, Supplementary Figure 13c & 14, NB5-2). Similarly, the difference in percent positive cells between each replicate was small (relative percent positive: mean=1.10, SEM=0.38, Supplementary Figure 13c, NB5-2). These data demonstrate reproducibility between batches, with the SBR of each antibody being stable, despite variations in raw intensity values (Supplementary Figure 9c, NB5-2). We used the same dataset to examine inter-patient variability on each TMA. The relative SBR between patients was often far from one (Supplementary Figure 13c, NB5-2), likely reflecting a combination of biological variability and pre-analytical factors that affect antibody performance in FFPE tissues.[26]

Since we observed intensity variation between CyCIF replicates, batch normalization was required for downstream analytics such as cell classification by unsupervised clustering. To quantify the effectiveness of batch correction methods on our serial TMA sections, we used the kBET algorithm[27], which, given a k-nearest neighbor graph, compares batch-label distribution in random subsets of neighboring cells to the global batch-label distribution, thus quantifying how well mixed batches are in technical replicates (Figure 5a, c, Supplementary Figure 15, NB5-3). Previously, we developed RESTORE, which utilizes mutually exclusive marker expression to predict a background threshold[28]. For normalization, we set all values below the RESTORE threshold to zero and scaled those above the threshold between 0 and 1. We compared RESTORE normalization to ComBat[29] and mean-only correction (regress out), both implemented in scanpy[30]. ComBat produced the best batch correction (kBET=0.45, SEM=0.05, n=3 slides, lower KBET rejection rates indicate better batch correction, with 0 being perfect mixing and 1 being no mixing of batches) with RESTORE also correcting some of the batch effect (kBET=0.62, SEM=0.03, Supplementary Figure 15, NB5-3). Unsupervised Leiden clustering showed that both ComBat and RESTORE recovered known biology (Supplementary Figure 15). To quantify the stability of clustering across batches, we calculated the Pearson correlation of the positive fraction of each cluster between each section (n=9; 3 cores x 3 sections). ComBat normalization produced higher correlation with lower variance (indicating fewer cores with low correlation) than RESTORE normalization, but both were improvements over the raw data (ComBat mean Pearson correlation=0.97, SEM=0.01, RESTORE mean=0.88, SEM=0.05, raw mean=0.8, SEM=0.15, n=9, Figure 5c, Supplementary Figure 15, NB5-4).

To further evaluate batch normalization methods, we created a TMA using FFPE breast cancer cell lines and normal tissues (Figure 5d). Importantly, the cell lines were of known clinical and intrinsic subtype[31], establishing a ground truth for clustering results (Supplementary Table 3). Three TMA sections were

stained using the same antibody conjugates but different panel orders (Supplementary Table 4). Images were processed through registration, autofluorescence subtraction, single cell segmentation, and feature extraction. Due to different panel orders, raw data showed significant batch effects, with little mixing of cells from different TMAs in a UMAP projection based on single cell marker intensity (Figure 3e, NB5-5). Again, the kBET algorithm[27] and replicates' cluster correlation were used to quantify the effectiveness of batch correction methods (Figure 5f, Supplementary Figure 16, NB5-6). Thirty methods were evaluated on three random samples of 600 cells from each core in each replicate (Supplementary Figure 16, NB5-5). Although Z-score normalization produced a reasonable kBET score (mean rejection rate=0.64, SEM=0.05, n=3), the UMAP did not show separation of each core, i.e. known breast cancer subtypes (Figure 5e, NB5-5). In contrast, the ComBat algorithm scored well with kBET (mean rejection rate=0.67, SEM=0.03, n=3), separated the cores in the UMAP, and clustering recovered known cell types within cell lines and normal tissues (Figure 5e, g, h). ComBat normalization applied without log2 transformation produced the most consistent clustering between replicate cores (mean Pearson correlation=0.97, SEM=0.06, 8 cores x 3 sections, n=24; Figure 5f, h, Supplementary Figure 16, NB5-5). RESTORE normalization resulted in improved cluster correlation compared to raw data (mean=0.73, SEM=0.25 versus mean=0.30, SEM=0.41, n=24), and recovered known biology (Figure 5f, Supplementary Figure 17, NB5-7); however, due to the lack of mutually exclusive marker pairs in cell lines, RESTORE did not perform as well as ComBat in this dataset (Figure 3f).

Since the ComBat normalization method[29] scored highest in kBET batch correction and cluster correlation in multiple datasets while recovering biological features of interest, we tested its sensitivity to different input distributions for parameterization. Since ComBat standardizes the mean and variance across batches, the same control tissue must be present in each batch (Figure 5i, j, Supplementary Figure 16e, f). Sampling cells from three control tissues (i.e. sampled training) produced better kBET scores

than using a single control tissue (sampled training with kBET=0.51, SEM=0.06 versus same training with kBET=0.79, SEM=0.07, n=3, Figure 5i, j, Supplementary Figure 16, NB5-3). Cluster correlation varied with the resolution of clustering, indicating higher precision batch correction with sampling from three rather than a single tissue (with 9 clusters, sampled training mean=0.98, SEM=0.02 versus same training mean=0.98, SEM=0.04; with 17 clusters, sampled training mean=0.97, SEM=0.02 versus same training mean= 0.94, SEM=0.05, n=9 Figure 5i, j, Supplementary Figure 16f). Therefore, one or more control tissues with similar cellular composition to the sample tissues should be included in each batch of CyCIF for proper ComBat normalization. In the absence of control tissues and given mutually-exclusive marker pairs, the RESTORE algorithm is a good alternative that produced high correlation in cluster composition in multiple replicate CyCIF experiments (mean correlation=0.88; 0.73). Additionally, in the absence of blank images for autofluorescence (AF) subtraction, RESTORE reduced the influence of AF on analytics (Supplementary Figure 15).

In summary, we performed extensive validation of the CyCIF multiplex imaging method to optimize fluorophore signal removal, antibody order and autofluorescence subtraction. We also quantified CyCIF similarity to standard IF and the reproducibility of staining, using this data to evaluate methods for batch normalization and cluster analysis to define biologically-relevant cell types. In parallel, we developed the open-source python library, mplexable, for reproducible image processing and analysis. We provided all of our code and data not only to document and reproduce our work, but to enable use and further community development of our analytics (https://github.com/engjen/cycIF_Validation). Our validation studies and computational tools will facilitate maturation of multiplex imaging methods towards quantitative, reproducible characterization of protein expression in intact tissue sections.

Methods

Tissue and Cell Button Preparation

We purchased TMA tissue sections (BR1506, US Biomax, Derwood, MD). All human tissue was collected under HIPPA approved protocols with the highest ethical standards with the donor being informed completely and with their consent (OHSU Biolibrary IRB 4918). Tissue blocks and tissue microarrays were from archival tissues fixed with standard methods (Biomax, Derwood, MD and OHSU Biolibrary, Portland, OR). Cell lines were cultured in conditions following Neve *et al*[31]. Cell line sources and culture media are as follows: AU565, ATCC, RPMI1640+10%FBS, BT474, ATCC, PMI1640+10%FBS, HCC1143, Adi Gazdar (now available through ATCC), RPMI1640+10%FBS, HCC3153, Adi Gazdar, RPMI1640+10%FBS, MDAMB436, ATCC, DMEM+10%FBS, T47D, ATCC, RPMI1640+10%FBS. FFPE cell buttons were prepared as previously described[32]. For each cell button, cells were scraped from two 15 cm plates and spun down (in 10 ml of culture media, no serum, for 4 min X 1000 rpm) in collodion-coated 15 ml glass centrifuge tubes (Fisher #C408-500). Collodion bags containing pellets were gently removed from tube, tied with thread, and transferred to 10% buffered formalin on ice. Cell pellets in collodion bags were fixed overnight at 4° C in 10% buffered formalin, then transferred through graded ethanol series (30%, 50%, 70%) for one hour each, and processed and embedded in paraffin. For cell line TMA creation, 1 mm cores from normal breast and tonsil (OHSU Biolibrary), or FFPE cell buttons were punched and inserted into the recipient block with the Estigen manual tissue arrayer MTA-1.

Cyclic Immunostaining

Formalin-fixed paraffin-embedded (FFPE) human tissues were sectioned at 4-5 microns and mounted on positively charged slides (Tanner Adhesive Slides, Mercedes Medical, TNR WHT45AD). The slides were baked overnight at 55 °C (Robbin Scientific, Model 1000) and for an additional 30 minutes at 65

°C, (Clinical Scientific Equipment NO. 100). Tissues were deparaffinized and hydrated through xylenes and graded ethanol (EtOH) as follows: xylenes (3 x 5 min), 100% EtOH (2 x 5 min), 95% EtOH (2 x 2 min), 70% EtOH (2 x 2 min), and distilled and deionized water (ddH_2O, 2 x 5 min). Two step antigen retrieval was performed in a Decloaking Chamber (Biocare Medical, Pacheco, CA) using the following settings: set point 1 (SP1), 125 °C, 30 seconds; SP2: 90 °C, 30 seconds; SP limit: 10 °C variation. Briefly, slides were placed in decloaking chamber in a plastic Coplin jar containing citrate buffer, pH 6 (10 mM citrate, Sigma C-1909). Two additional polyethylene Coplin jars with buffer were placed in chamber to heat, which contained ddH_2O and 1x Target Retrieval Solution, pH 9 (Agilent S2367). The chamber was heated to 125 °C, held for 30 seconds (SP1), then cooled to 90 °C, 0 psi and held for 30 seconds (SP2). After the SP2 program was completed, the decloaking chamber was turned off, opened, and slides were dipped in the Coplin jar containing hot ddH_2O for ~1 second. Slides were then transferred to hot 1x Target Retrieval Solution pH 9. The lid was placed back on chamber, and slides remained in hot pH 9 buffer for 15 minutes. Following this two-step antigen retrieval, the tissues were washed in two brief changes of ddH_2O (~2 seconds) and then washed once for 5 minutes in 1x phosphate buffered saline (PBS), pH 7.4 (Fisher, BP39920).

Pre-quenching to reduce autofluorescence

Next, pre-quenching was performed on tissues to reduce tissue autofluorescence. Quenching solution containing 20 mM sodium hydroxide (NaOH) and 3% hydrogen peroxide (H_2O_2) in 1x PBS was freshly prepared from stock solutions of 5 M NaOH and 30% H_2O_2, and each slide was placed in 10 ml quenching solution. Slides were quenched face down on ~1 mm risers in a 4-well rectangular tissue culture dish (each well holds one slide), under incandescent light, for 30 minutes. Lamps with 60-Watt incandescent bulbs were positioned so the bulb was four inches above the 4-well dish. Placing slides in the outer two wells and leaving the center wells empty resulted in the temperature increasing from 23° C

to 39° C over 30 minutes (see Supplementary Figure 5c). Slides were then removed from the chamber with forceps and washed 3 x 2 min in 1x PBS. Sections were blocked in 10% normal goat serum (NGS, Vector S-1000) and 1% bovine serum albumin (BSA, Sigma A7906) in 1x PBS for 30 minutes at room temperature in a humidified chamber. Plastic cover slips (IHC World, IW-2601) were used to spread blocking solution evenly across tissue. Tissues were soaked briefly in PBS in a Coplin jar to remove plastic coverslip, then washed 1 x 5 min in PBS. Coverslips (Corning; 2980-243 and 2980-245) were mounted in Slowfade Gold plus DAPI mounting media (Life Technologies, S36938). Pre-staining autofluorescence signal was acquired using a Zeiss Axioscan Z.1 (see imaging protocol below). After acquiring autofluorescence signal, slides were soaked in 1x PBS for 10 – 30 minutes in a glass Coplin jar, waiting until glass coverslip slid off without agitation.

Primary Antibody Staining

Primary antibodies were diluted in 5% NGS and 1% BSA in 1x PBS (see Supplementary Data 1) and applied overnight at 4 °C in a humidified chamber, covered with plastic coverslips (IHC World, IW-2601). Following overnight incubation, tissues were washed 3 x 10 min in 1x PBS, and coverslipped as described above. Antibody information is provided in Supplementary Data 1.

Fluorescence Microscopy

For standard versus CyCIF and reproducibility experiments, fluorescently stained slides were scanned on the Zeiss AxioScan.Z1 (Zeiss, Germany) with a Lumencor SpectraX-IR light source (Lumencor Inc., Beaverton, OR). The filter cubes used for image collection were DAPI (Semrock, LED-DAPI-A-000), AF488 (Zeiss 38 HE), AF555 (Zeiss 43 HE), AF647 (Zeiss 50) and Alexa Fluor 750 (AF750, Chroma 49007 ET Cy7). The exposure time was determined individually for each slide and stain, and the LED light intensity was fixed at 100%. Full tissue scans were taken with the 20x objective and stitching was

performed in Zen Blue image acquisition software (Zeiss). After those initial experiments, a new light source was purchased and used for collecting quenching and round order data. For those experiments, a Colibri 7 light source (Zeiss), with the same filter cubes, except DAPI (Zeiss 96 HE), was used. The exposure time was determined individually for each slide and stain to ensure maximum dynamic range without saturation, and the LED light intensity was fixed at 10% (DAPI), 20% (AF488), and 50% (AF555, AF647, AF750). Full tissue scans were taken with the 20x objective (Plan-Apochromat 0.8NA WD=0.55, Zeiss) and stitching was performed.

Quenching of Fluorescence Signal for Cyclic Immunostaining.

After successful scanning, slides were soaked in 1x PBS for 10 – 30 minutes in a glass Coplin jar, waiting until glass coverslip slid off without agitation. Quenching was performed as described above, in the section of Pre-quenching to reduce autofluorescence. After removal from quenching solution, slides were washed 1 x 5 min in 1x PBS and subsequent rounds of primary antibodies were applied, diluted in blocking buffer as described in the section of Primary Antibody Staining.

Image Registration, Autofluorescence Removal and Segmentation

Scanned images were first split into separate scenes using the function Split Scenes (Write files) in Zeiss Zen Blue software (with "Include scene information in the Generated File name" unchecked). For the datasets used in this work, we did not apply flat field correction, although it may be applied in Zen using the function Shading Correction. Using the same software, each scene was then exported to 16-bit grayscale uncompressed TIFF using the function Image Export. Quality control and metadata extraction were performed in python. TIFF images from each round of cyclic immunostaining were registered based on DAPI staining as follows. Image features were found with the detectSURFFeatures function, and automated feature matching was performed with the matchFeatures function, in Matlab (R2017B

9.3.0.713579, MathWorks, Natick, MA). Image registration was the performed using Matlab' estimateGeometricTransform function and performing affine registration (scaling, rotation, translation). Although Matlab was used for the majority of registration in this work, we also successfully registered images using a python implementation. Both scripts are provided (Matlab: https://gitlab.com/engje/mplexable/-/blob/master/mplexable/src/template_registration_mscene.m and python: https://gitlab.com/engje/mplexable/-/blob/master/mplexable/src/template_registration_mscene.py).

Autofluorescence subtraction preceded segmentation. Images of unstained tissue were acquired in each channel, before and after staining. For each marker, background images were scaled linearly by exposure time and relative round, and subtracted using mplexable.

Deep learning based cell segmentation was performed with Cellpose, a generalist algorithm for cellular segmentation[33]. Cellpose was used to generate nuclear and cell masks by classifying pixels on the basis of a DAPI or E-cadherin antibody staining, respectively. The following parameters were used for Cellpose segmentation: for the cells, diameter=30 pixels, flow_threshold=0.6, min_size=113; for the nuclei, diameter=30, flow_threshold=0, min_size=28. Nuclei with no E-cadherin (Ecad) staining (i.e., non-epithelial cells) were expanded by 5 pixels (1.6 micrometers) to approximate the cytoplasm, based on the average measurement of immune cell cytoplasm in images. The cytoplasm was derived by subtracting the nuclei area from the cell segmentation result, or from the 5-pixel expansion result in the case of Ecad negative cells. The mean intensity of each subcellular region was extracted using mplexable. Watershed-algorithm-based cell segmentation was performed for some datasets, using in-house java software for the following operations. A z-projection of DAPI images from all rounds of staining was processed with the white top-hat algorithm that separates individual nuclear candidates from the background. Contours of nuclei were detected with the Prewitt operator, and single nuclei were segmented by applying a watershed algorithm to the nuclear contours, with top-hat candidates as seeds.

Nuclear segmentation accuracy was improved by sorting nuclei based on expression of tumor cytokeratins or immune markers and using this information to set a maximum nuclear size for the watershed algorithm. If a cell was positive for cytokeratins, it was allowed to have a larger nucleus than cells that were negative for cytokeratins because it was assumed to be an epithelial cell. Cell segmentation was achieved by applying a watershed on the Ecad image with segmented nuclei as seeds, or by inflating the nuclei if the Ecad marker was negative. The resulting segmentation mask defined nuclear and cytoplasmic regions for each cell. Mean intensity used for downstream analysis was selected for each marker based on its biologically-relevant subcellular region (e.g., cytoplasm for CK19, nuclei for Ki67).

Data Analysis

For single cell analyses, single cell mean intensity was used for clustering, as in Figure 4 and 5. For percent positive calculation, as in Figure 2c (left), cells with a mean intensity above threshold were considered positive. Tissue retention was calculated in Figure 2e – h by thresholding DAPI using the Li algorithm[34] and considering cells above DAPI threshold as retained in that round. For signal-to-background (SBR) calculations, mean intensity was integrated across the entire slide or region of interest, as in Figure 2c, right, Figure 3, and Figure 5b. In fluorescence imaging, background adds to the signal of interest[35], so SBR was calculated as *(mean intensity of positive pixels – mean intensity of negative pixels) / mean intensity of negative pixels* (NB2-1). For SBR quantification in Figure 2, thresholds were applied directly to image data (no single cell segmentation) and signal was taken as the mean pixel intensity above the threshold, while background was defined as the mean pixel intensity of pixels below the threshold and 30 pixels away (10 μm) from the positive pixels to exclude the influence of lateral bleed through. Since the threshold directly determines the result, thresholds were used that selected a similar pixel pattern and area in adjacent sections. The same marker in adjacent sections was

visualized side-by-side, and the respective thresholds were adjusted until the positive pixels were as equivalent as possible, which was estimated by eye. Therefore, although the threshold reflected the subjective decision of the researcher, it allowed comparison of similar pixels in replicates across adjacent sections. The masks that resulted from thresholding are provided for visual assessment of thresholds (https://github.com/engjen/cycIF_Validation/blob/master/Extended_single_vs_cyclic.ipynb and https://github.com/engjen/cycIF_Validation/blob/master/Extended_Reproducibility_3TMA_Tissue.ipynb).

We tested whether the same threshold could be applied to different regions of the same slide by measuring correlation between two ROIs in normal breast and two ROIs in HER2+ breast tumor given the same threshold. The mean fluorescence intensity measured above threshold, and the intensity of background noise were highly correlated between ROIs (Supplementary Figure 2). Finally, we tested whether manual thresholds gave us a different answer for SBR calculations than estimating SBR at the $95^{th}/5^{th}$ quantile (Supplementary Figure 14).

Dynamic range was estimated using the 4th and 99.5^{th} quantile of mean intensity for markers in tissues with known positive staining. We compared different ranges for estimating dynamic range (5th to 98th percentile versus 5th to 99.9 percentile, see Supplementary Figure 14). We found that using a higher maximum did not change the dynamic range as much for common markers (e.g., CK7) but had more effect on rare markers (e.g., Ki67 and alpha-SMA). Therefore, we selected the 99.5^{th} percentile as the maximum to reflect both common and rare markers' dynamic range. In cases where we did not set a manual threshold, SBR was estimated as the ratio of the (99.5th quantile – 4th quantile)/4th quantile of mean intensity.

For SBR quantification in Figure 3, we needed to calculate SBR in the presence of artifacts such as non-specific staining, bleed through, autofluorescence and incomplete quenching. We utilized the

napari image viewer to overlay all of the markers, set thresholds and create masks. For positive signal, we set a threshold (recorded in our 20211007_napari.py script) that created a mask including all of the positive staining plus any bright artifacts. We then manually erased areas of the mask covering imaging or staining artifacts and saved the mask for future reproducibility. For background signal, we manually selected six regions of the image exhibiting background caused by the artifacts listed above, and again saved the mask. We then extracted the mean intensity of the positive and background areas of the image and used these to calculate SBR as described above.

For F1 score calculation in Supplementary Figure 11, we again used the napari image viewer to overlay staining, segmentation results, and positive cells based on manual thresholding. Based on the staining pattern and other marker's expression (e.g., membranous CD8 staining in CD45+ cells was a true CD8 positive), we manually annotated false negatives in three 2000 x 2000-pixel ROIs. False positives were any cell with AF488 autofluorescence >1024-pixel intensity, true positives were cells above this threshold excluding false positives and true negatives were all other cells neither positive, false positive or false negative.

Normalization methods tested included transformations (raw, log2 or arcsinh), division by background signal, determined either with RESTORE, which requires mutually exclusive marker expression in different cell populations, or the 3rd quantile of background fluorescence measured in the reverse subcellular compartment of expected localization (e.g., cytoplasmic signal for nuclear markers), scaling methods (standard, min-max, max-abs, robust, quantile and power) which are implemented in the python library scikit-learn[36] and batch correction algorithms regress_out and ComBat, implemented in the python library scanpy[30]. For RESTORE normalization, the scikit-learn[36] TruncatedSVD decomposition function was used to quantify the L-shaped distribution of marker pairs; in each core, markers were considered mutually exclusive if the function yielded an R-value above 0.5, or above 0.2 when no pairs reached the 0.5 cut-off. For global thresholds, a more stringent cutoff was used (for the

presented TMA datasets 0.66 globally or 0.5 when no pairs reached the 0.66 cut-off. For each core or batch, this procedure generated data-driven mutually exclusive marker pairs. The selected mutually exclusive marker pairs were used to calculate RESTORE thresholds, and the median threshold produced by multiple marker pairs was selected for normalization. Mean intensity was normalized with division by local (per core) and global (per batch) thresholds. For the RESTORE scale method, cells with intensity below threshold were set to a random value between 0 and 0.02, while all cells with intensity above threshold were scaled to a range of 0.02 – 1 for each marker.

Following normalization, 7200 cells (cell lines) or 5400 cells (tissues) were randomly sampled (i.e., 600 cells per TMA core from each batch) and evaluated for batch effects using the kBET algorithm[27] (n=3). UMAP visualization and graph-based Leiden clustering (resolution=0.6) was carried out using scanpy[30].

Statistics and Reproducibility

All visualizations and results can be fully reproduced from the raw images with the accompanying code and data, here https://github.com/engjen/cycIF_Validation. Statistical analyses were conducted in python using the scipy[37] library. Replicates were defined as separate CyCIF experiments. Sample sizes are defined by the number of tissues stained, including tissue cores in TMAs.

Data Availability

All image data is available at synapse.org, at cycIF_Validation, syn23644107. The synapse platform requires registration. With a free account, the images are freely accessible. All other source data used to produce the graphs and figures is available here: https://github.com/engjen/cycIF_Validation, DOI: 10.5281/zenodo.6049278.

Code Availability

The data, code and Jupyter notebooks to reproduce the analyses herein are at https://github.com/engjen/cycIF_Validation, DOI: 10.5281/zenodo.6049278. For image processing, we developed mplexable, available through the Python Package Index, https://pypi.org/project/mplexable/. An image processing tutorial with Zeiss Axioscan example images is available at https://www.synapse.org/#!Synapse:syn26958265. Additionally, we demonstrate processing Zeiss Axioscan, Akoya CODEX and Miltenyi MACSima prototype images in our pipeline example Jupyter notebooks, here: https://gitlab.com/engje/mplexable/-/tree/master/jupyter.

Competing Interests

J.W.G. has licensed technologies to Abbott Diagnostics; has ownership positions in Convergent Genomics, Health Technology Innovations, Zorro Bio, and PDX Pharmaceuticals; serves as a paid consultant to New Leaf Ventures; has received research support from Thermo Fisher Scientific (formerly FEI), Zeiss, Miltenyi Biotech, Cepheid (Danaher), Quantitative Imaging, Health Technology Innovations, and Micron Technologies; and owns stock in Abbott Diagnostics, AbbVie, Alphabet, Amazon, Amgen, Apple, General Electric, Gilead, Intel, Microsoft, Nvidia, and Zimmer Biomet. S.L.G. has received research support from Quantitative Imaging. The remaining authors declare no competing interests.

Acknowledgments

We would like to thank former lab members Dr. Moqing Liu, Aesoon Bensen and Lydia Grace Campbell as well as former interns Clayton Peltz and Cole Meyer for assistance with staining and imaging. We would also like to thank Damir Sudar for technical support related to image storage. We appreciate the sample scanning assistance of both Drs. Stefanie Kaech Petrie and Crystal Chaw at the OHSU Advance Light Microscopy Core. The OHSU Biolibrary and OHSU Histopathology Share

Resource provided tissue blocks and histology services. We would like to thank Elliot Gray for assistance with python and shell scripts. We would like to thank Drs. Andreas Bosio and Werner Muller for insightful discussions on the Miltenyi MACSima prototype image analysis. The Miltenyi MACSima Prototype instrument was provided by Miltenyi. Drs. Young Hwan Change and Erik Burlingame contributed ideas for data analysis and image visualization as well as code for RESTORE normalization and registration. Dr. Guillaume Thibault provided the code for watershed segmentation. This work was supported by funding from the Prospect Creek Foundation, Susan G. Komen Foundation, OHSU Foundation. Additionally, J.W.G acknowledges support from NIH/NCI U54 CA209988, NCI SBIR 1R44CA224994-01, NIH/NCI U2C CA233280. The OHSU Knight Cancer Institute Shared Resources are supported by the Knight Cancer Institute Cancer Center Support Grant (NIH/NCI P30CA69533).

Author Contributions

Jennifer Eng, Summer L. Gibbs, Koei Chin and Joe W. Gray conceived of the project.

J.E. and K.C. designed the antibody panel, performed experiments and processed image data.

J.E and Elmar Bucher developed free and open-source python tools and Jupyter notebooks for image processing, visualization and analysis.

Zhi Hu performed staining and imaging experiments.

Ting Zheng established quenching and antibody labeling protocols.

J.E. drafted the manuscript and prepared the figures.

S.L.G, K.C and J.W.G directed the project and edited the manuscript.

References

1. Carstens, J. L. *et al.* Spatial computation of intratumoral T cells correlates with survival of patients with pancreatic cancer. *Nat. Commun.* **8**, 1–13 (2017).

2. Viratham Pulsawatdi, A. *et al.* A robust multiplex immunofluorescence and digital pathology workflow for the characterisation of the tumour immune microenvironment. *Mol. Oncol.* **14**, 2384–2402 (2020).

3. Zhang, W. *et al.* Fully automated 5-plex fluorescent immunohistochemistry with tyramide signal amplification and same species antibodies. *Lab. Investig.* **97**, 873–885 (2017).

4. Tsujikawa, T. *et al.* Quantitative Multiplex Immunohistochemistry Reveals Myeloid-Inflamed Tumor-Immune Complexity Associated with Poor Prognosis. *Cell Rep.* **19**, 203–217 (2017).

5. Banik, G. *et al. High-dimensional multiplexed immunohistochemical characterization of immune contexture in human cancers*. *Methods in Enzymology* **635**, (Elsevier Inc., 2020).

6. Gut, G., Herrmann, M. D. & Pelkmans, L. Multiplexed protein maps link subcellular organization to cellular states. *Science (80-.).* **361**, (2018).

7. Bolognesi, M. M. *et al.* Multiplex Staining by Sequential Immunostaining and Antibody Removal on Routine Tissue Sections. *J. Histochem. Cytochem.* **65**, 431–444 (2017).

8. Cattoretti, G., Cattoretti, G., Bosisio, F. M., Marcelis, L. & Bolognesi, M. M. Multiple Iteractive Labeling by Antibody Neodeposition (MILAN). *Protoc. Exch.* 1–12 (2018). doi:10.1038/protex.2018.106

9. Lin, J. R., Fallahi-Sichani, M. & Sorger, P. K. Highly multiplexed imaging of single cells using a high-throughput cyclic immunofluorescence method. *Nat. Commun.* **6**, 1–7 (2015).

10. Lin, J.-R. *et al.* A simple open-source method for highly multiplexed imaging of single cells in tissues and tumours. *Elife* **7**, 151738 (2018).

11. Eng, J. *et al.* Cyclic Multiplexed-Immunofluorescence (cmIF), a Highly Multiplexed Method for Single-Cell Analysis. in *Biomarkers for Immunotherapy of Cancer. Methods in Molecular Biology* (eds. Thurin, M., Cesano, A. & Marincola, F. M.) **2055**, 521–562 (Humana, 2020).

12. Gerdes, M. J., Sevinsky, C. J., Sood, A., Adak, S. & Bello, M. O. Highly multiplexed single-cell

analysis of formalin-fixed, paraffin-embedded cancer tissue. *Proc. Natl. Acad. Sci. U. S. A.* **110**, 11982–11987 (2013).

13. Radtke, A. J. *et al.* IBEX: A versatile multiplex optical imaging approach for deep phenotyping and spatial analysis of cells in complex tissues. *Proc. Natl. Acad. Sci. U. S. A.* **117**, 33455–33465 (2020).
14. Schubert, W. *et al.* Analyzing proteome topology and function by automated multidimensional fluorescence microscopy. *Nat. Biotechnol.* **24**, 1270–1278 (2006).
15. Pascual-Reguant, A. *et al.* Multiplexed histology analyses for the phenotypic and spatial characterization of human innate lymphoid cells. *Nat. Commun.* **12**, 1–15 (2021).
16. Goltsev, Y. *et al.* Deep Profiling of Mouse Splenic Architecture with CODEX Multiplexed Imaging. *Cell* **174**, 968-981.e15 (2018).
17. Manesse, M., Katir K. Patel, Bobrow, M. & Downing, S. R. The InSituPlex® Staining Method for Multiplexed Immunofluorescence Cell Phenotyping and Spatial Profiling of Tumor FFPE Samples. in *Biomarkers for Immunotherapy of Cancer. Methods in Molecular Biology* (eds. Thurin, M., Cesano, A. & Marincola, F. M.) **2055**, 625–626 (Humana, 2020).
18. Saka, S. K. *et al.* Immuno-SABER enables highly multiplexed and amplified protein imaging in tissues. *Nat. Biotechnol.* **37**, 1080–1090 (2019).
19. McMahon, N. P. *et al.* Oligonucleotide conjugated antibodies permit highly multiplexed immunofluorescence for future use in clinical histopathology. *J. Biomed. Opt.* **25**, 1 (2020).
20. Giesen, C. *et al.* Highly multiplexed imaging of tumor tissues with subcellular resolution by mass cytometry. *Nat. Methods* **11**, 417–422 (2014).
21. Keren, L. *et al.* A Structure Tumor-Immune Microenvironment in Triple Negative Breast Cancer Revealed by Multiplexed Ion Beam imaging. *Cell* **174**, 1373-1387.e19 (2018).
22. Stewart, R. L., Matynia, A. P., Factor, R. E. & Varley, K. E. Spatially-resolved quantification of

proteins in triple negative breast cancers reveals differences in the immune microenvironment associated with prognosis. *Sci. Rep.* **10**, 1–8 (2020).

23. McGinnis, L. M., Ibarra-Lopez, V., Rost, S. & Ziai, J. Clinical and research applications of multiplexed immunohistochemistry and in situ hybridization. *J. Pathol.* **254**, 405–417 (2021).

24. Du, Z. *et al.* Qualifying antibodies for image-based immune profiling and multiplexed tissue imaging. *Nat. Protoc.* **14**, 2900–2930 (2019).

25. Gambella, A. *et al.* Section detachment in immunohistochemistry: causes, troubleshooting, and problem-solving. *Histochem. Cell Biol.* **148**, 95–101 (2017).

26. Bass, B. P., Engel, K. B., Greytak, S. R. & Moore, H. M. A review of preanalytical factors affecting molecular, protein, and morphological analysis of Formalin-Fixed, Paraffin-Embedded (FFPE) tissue: How well do you know your FFPE specimen? *Arch. Pathol. Lab. Med.* **138**, 1520–1530 (2014).

27. Büttner, M., Miao, Z., Wolf, F. A., Teichmann, S. A. & Theis, F. J. A test metric for assessing single-cell RNA-seq batch correction. *Nat. Methods* **16**, 43–49 (2019).

28. Chang, Y. H. *et al.* RESTORE: Robust intEnSiTy nORmalization mEthod for multiplexed imaging. *Commun. Biol.* **3**, 1–9 (2020).

29. Johnson, W. E., Li, C. & Rabinovic, A. Adjusting batch effects in microarray expression data using empirical Bayes methods. *Biostatistics* **8**, 118–127 (2007).

30. Wolf, A., Angerer, P. & Theis, F. SCANPY: large-scale single-cell gene expression data analysis. *Genome Biol.* **19**, (2018).

31. Neve, R. M. *et al.* A collection of breast cancer cell lines for the study of functionally distinct cancer subtypes. *Cancer Cell* **10**, 515–527 (2006).

32. Balassanian, R. *et al.* A superior method for cell block preparation for fine-needle aspiration biopsies. *Cancer Cytopathol.* **124**, 508–518 (2016).

33. Stringer, C., Wang, T., Michaelos, M. & Pachitariu, M. Cellpose: a generalist algorithm for cellular segmentation. *Nat. Methods* **18**, 100–106 (2021).

34. Li, C. H. & Tam, P. K. S. An iterative algorithm for minimum cross entropy thresholding. *Pattern Recognit. Lett.* **19**, 771–776 (1998).

35. Waters, J. C. Accuracy and precision in quantitative fluorescence microscopy. *J. Cell Biol.* **185**, 1135–1148 (2009).

36. Pedregosa, F. *et al.* Scikit-learn: Machine Learning in Python Fabian. *J. Mach. Learn. Res.* **12**, 2825–2830 (2011).

37. Virtanen, P. *et al.* SciPy 1.0: fundamental algorithms for scientific computing in Python. *Nat. Methods* **17**, 261–272 (2020).

Figure Legends

Figure 1. Reproducible Generation, Processing and Analysis of Multiplex Images. a. CyCIF data is generated with a reproducible protocol (dx.doi.org/10.17504/protocols.io.3xfgpjn). b. Image processing pipeline integrates quality control and workflow management with in-house Python software, mplexable, facilitating data quality, scaling and reproducibility. c. Analysis, image visualization and figure generation are fully reproducible with shared linked and executable code and data. Raw and processed data, metadata and analysis are documented in Jupyter notebooks running our free and open-source software that provides a framework for reproducible image analysis.

Figure 2: CycIF Signal to Background and Tissue Loss. Comparison of CyCIF staining to a standard IF protocol, in adjacent sections of HER2+ tumor and normal breast tissue. a. Multicolor visualizations are produced with our python code. b. Positive pixels, or foreground (FG), were determined by thresholding and negative pixels, or background (BG), were determined by selecting regions 10 µm away from positive regions. The signal-to-background ratio (SBR) is the mean intensity of FG/mean intensity of BG. c. Positive cell counts were determined by applying the thresholds from (b) to single cell mean intensities of segmented cells. Pearson correlation (R), was calculated for standard IF versus CyCIF fraction positive in tissue and SBR, n=26; R and p-value given in figure title. d. Three adjacent sections of a 72-core tissue microarray (TMA) containing normal and malignant tissues were repeatedly quenched to assess tissue loss during CyCIF. e. Tissue retention after each round of quenching. Error is 95% confidence interval of tissue retention at each round for normal, benign and malignant tissues, n = 54, 6 and 156, respectively (18 normal, 2 benign and 52 malignant tissues x 3 replicate TMAs). f. Fraction of cells remaining after 10 rounds of CyCIF, separated by type, stage, grade and source. g. Tissue retention by nuclear area quartile; error is 95% confidence interval, n=216 cores. h. Fraction of cells remaining after 10 rounds of CyCIF, separated by nuclear area quartile and nuclear eccentricity quartile. In f, h, Kruskal-Wallis H-test was used to assess differences in tissue retention, n = 216 (72 cores x 3 replicate TMAs), except Source, which includes only normal tissue, n=41 cores. p-value shown in figure title. In a-b, scale bar = 50 µm.

Figure 3. CyCIF Optimization: Quenching and Panel Order. a-d. Quenching Optimization. a. Normal pancreas was stained with CK7-AF488 and imaged before and after fifteen minutes of quenching in 3% (top row), 4.5% (middle row) or 6% (bottom row) H_2O_2. b. Breast cancer tissue stained with CK7-AF488 and Vimentin-AF488 imaged before and after 30 (top) and 60 minutes of quenching (bottom). c. Tissue stained as in (b) and imaged before and after 30-minute quenching under incandescent light source. d. Mean AF488 (left) or AF555 (right) fluorescence intensity in tissue area of stained tissue relative to a blank autofluorescence control after one round of quenching with conditions shown in a-c. e - h. Panel order optimization, with representative images. i. Signal-to-background ratio (SBR) quantification was done by applying a threshold to find positive pixels, and manually selecting areas of non-specific background, e.g., tumor nests in e-g and stromal areas in h., n=6 areas per tissue. A t-test was used to assess significance; p-value shown in figure title. e. Non-specific nuclear staining in

the AF750 channel is improved by moving antibody to a later round. CD45-AF750 showed higher SBR in round (R) 6 than in R2. f. Autofluorescence in the AF55 or AF488 channel is mitigated by moving antibody from R1 to a later round. CD8-AF555 had higher SBR in R7 than R1. g. Channel bleed through is mitigated by pairing two bright or two dim antibodies in adjacent channels, not a bright with a dim. PD1-AF647 shows bleed through from bright CK19-AF750 in R1, but not from CD45-AF750 in R6. h. Incomplete quenching is mitigated by moving markers resistant to quenching to later in the panel. Vimentin-AF488 resists quenching and is moved after cytokeratin staining, rather than before. j. Schematic of panel optimizations addressing background and dynamic range, autofluorescence, channel bleed-through and incomplete quenching. a-c & e-h. Blue = DAPI, Green = Stain, green colorbar = 16-bit grayscale intensity, Y-axis scale is in micrometers, scale bar = 30 µm.

Figure 4. Autofluorescence Characterization in the CyCIF Protocol. a. Top: DAPI nuclear staining and autofluorescence in the AF488 channel before and after 60 minutes of quenching. Arrowheads show areas of bright (gray), medium (purple) and dim (pink) autofluorescence. Bottom: Colored nuclei of clusters 7 (left), 4 (middle) and 6 (right) on the autofluorescence image, representing cells with bright (gray arrowhead), medium (purple arrowhead) and dim (pink arrowhead) autofluorescence, respectively. Scale bar = 30 µm. b. UMAP projection of single cells based on autofluorescence, colored by AF488 intensity after 0 or 60 minutes of quenching (left and middle); Umap colored by unsupervised clustering results of the Leiden algorithm (right). c. Mean AF488 intensity of cells in each Leiden cluster over rounds of quenching; note bright (gray line) cells quench differently than medium (purple line) and dim (pink line) cells. Similar trend in nuclear (left) and cytoplasmic (right) autofluorescence, although nuclear is brighter. d. Autofluorescence analysis as in (a-c) was repeated on a 72-core tissue microarray (TMA). AF488 autofluorescence shown after 0 minutes (top) and 330 minutes or quenching (bottom). e. UMAP projection of single cells based on autofluorescence, colored by AF488 intensity after 0 (top) or 330 minutes of quenching (bottom). f. UMAP colored by batch. Three adjacent sections from TMA were repeatedly quenched and normalized by batch for analysis. g. UMAP colored by unsupervised clustering results of the Leiden algorithm. h. Mean AF488 intensity of cells in each Leiden cluster over rounds of quenching. Overall, minimum intensity was observed at 120 minutes and maximum intensity at 240 minutes. i. Subtracting the minimum intensity autofluorescence will avoid over-subtraction while still removing 60 - 70% of autofluorescence at 240 minutes. j. Heatmap showing observed number of cells per Leiden cluster – expected number of cells per cluster, by tissue, y-axis, illustrating different trends by tissue. Brightest autofluorescence, cluster 14 (yellow line, h), originates from liver tissue. Cluster 10, showing greatest fraction of autofluorescence remaining after subtraction (blue bar, i), originates primarily in lymph node. c, h and i. Error bars = standard error of the mean, n=3 slides.

Figure 5. Reproducibility and Normalization of CyCIF Staining Intensity. a. Representative images, generated with our python code, of 12 markers from three adjacent sections of a breast cancer TMA stained with a 20-marker CyCIF panel, scale bar = 50 µm. b. Relative SBR of slide 1-2, 2-3 and 1-3 for each marker. c. Evaluation of batch correction with kBET (left, lower rejection rates indicating better batch correction, n=3 batches, 5400 cells) and correlation (Pearson, n=9) of Leiden cluster composition between replicate cores for different batch correction methods (right) d. Overview of breast cancer cell line and normal tissue TMA created to represent breast cancer subtypes. e. UMAP projection based on single-cell marker intensity; left to right: raw data, z-score normalization and ComBat normalization, colored by batch (top) and TMA core/cell line (bottom). f. Evaluation of batch correction with kBET (left, n=3 batches, 7200 cells) and cluster correlation (right, n=24) on cell line TMA. g. Heat map of relative mean intensity of each marker in the ComBat normalized, Leiden-clustered cell line TMA data, with annotation on left. h. Fraction of cells in each cluster from (g), showing similar composition of technical replicates and reflecting known normal tissue and cell line cell types. i. Schematic of different

selection methods to parameterize the ComBat algorithm. j. Evaluation of ComBat parameterization with kBET (left, n=3 batches, 7200 cells) and cluster correlation (right, n=9). c, f and j. Error bars = standard error of the mean, n=3 slides.

Table 1: Links to Analysis Notebooks	
Name	url
NB1-1	https://github.com/engjen/cycIF_Validation/blob/master/Multicolor_Image_Visualization.ipynb
NB2-1	https://github.com/engjen/cycIF_Validation/blob/master/Extended_single_vs_cyclic.ipynb
NB2-2	https://github.com/engjen/cycIF_Validation/blob/master/SinglevsCyclic_44290.ipynb
NB3-1	https://github.com/engjen/cycIF_Validation/blob/master/Quenching_analysis.ipynb
NB3-3	https://github.com/engjen/cycIF_Validation/blob/master/Image_Analysis_Visualization.ipynb
NB3-4	https://github.com/engjen/cycIF_Validation/blob/master/DoubleApplication_K157.ipynb
NB3-5	https://github.com/engjen/cycIF_Validation/blob/master/OrderOptimization_K154vsK175.ipynb
NB3-6	https://github.com/engjen/cycIF_Validation/blob/master/Macsima_clustering.ipynb
NB4-1	https://github.com/engjen/cycIF_Validation/blob/master/Quenching_Single_Cell.ipynb
NB5-1	https://github.com/engjen/cycIF_Validation/blob/master/Extended_Reproducibility_3TMA_Tissue.ipynb
NB5-2	https://github.com/engjen/cycIF_Validation/blob/master/TMAReplicates_analysis.ipynb
NB5-3	https://github.com/engjen/cycIF_Validation/blob/master/Normalization_testing_tissue.ipynb
NB5-4	https://github.com/engjen/cycIF_Validation/blob/master/Normalization_testing_HER2-N75.ipynb
NB5-5	https://github.com/engjen/cycIF_Validation/blob/master/Normalization_testing.ipynb
NB5-6	https://github.com/engjen/cycIF_Validation/blob/master/kBET.ipynb
NB5-7	https://github.com/engjen/cycIF_Validation/blob/master/RestoreNorm_scale.ipynb

Table 1. Reproducible Image Analytics. All figures and results can be fully reproduced with the accompanying Jupyter notebooks and data provided here: https://github.com/engjen/cycIF_Validation,

DOI: 10.5281/zenodo.6049278

a Protocol: Reproducible Methods

CyCIF Staining, Imaging and Quenching

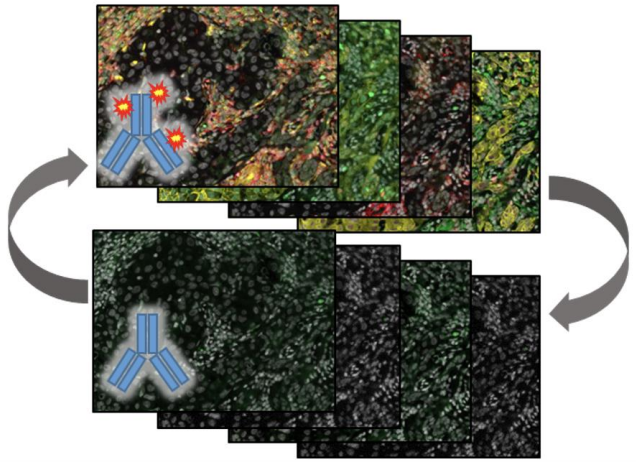

dx.doi.org/10.17504/protocols.io.3xfgpjn

b Pipeline: Quality Control & Workflow Management

Multiplex Image QC

- Automated Visualization

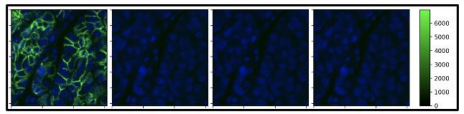

- Metadata Extraction

BIO-FORMATS

- Error Correction

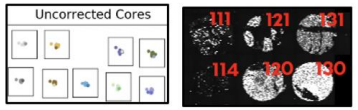

gitlab.com/engje/mplexable

Image Processing Pipeline

- Image Registration

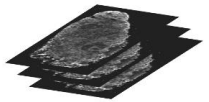

MATLAB

- Cell Segmentation

cellpose

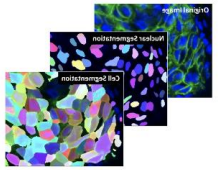

- Feature Extraction

python

c Analytics: Linked and Executable Code and Data

Raw Image Data SYNAPSE

Processed Data and Results

Data Description

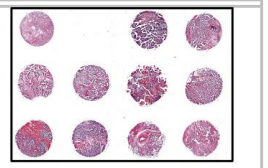

- Samples
- Treatments
- Staining conditions
- Image metadata
  - Markers
  - Exposure time

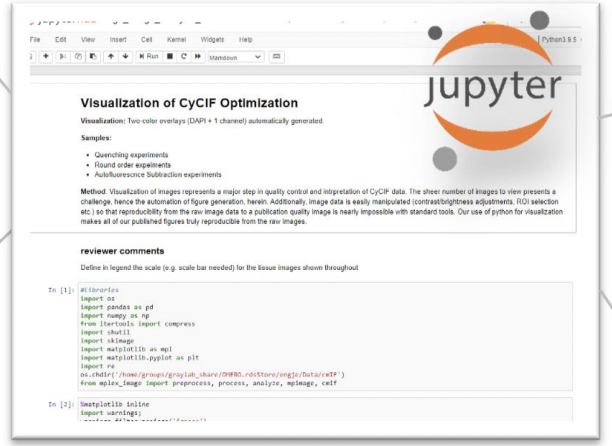

Documentation of Analysis

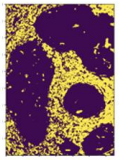

- Representative image selection
- Region of interest selection
- Display range
- Thresholds and masks
- Parameter selection

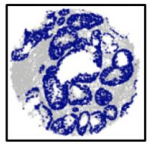

Computational Environment

- Free and open source software
- Zero-install option

binder

github.com/engjen/cycIF_Validation

Fig. 1

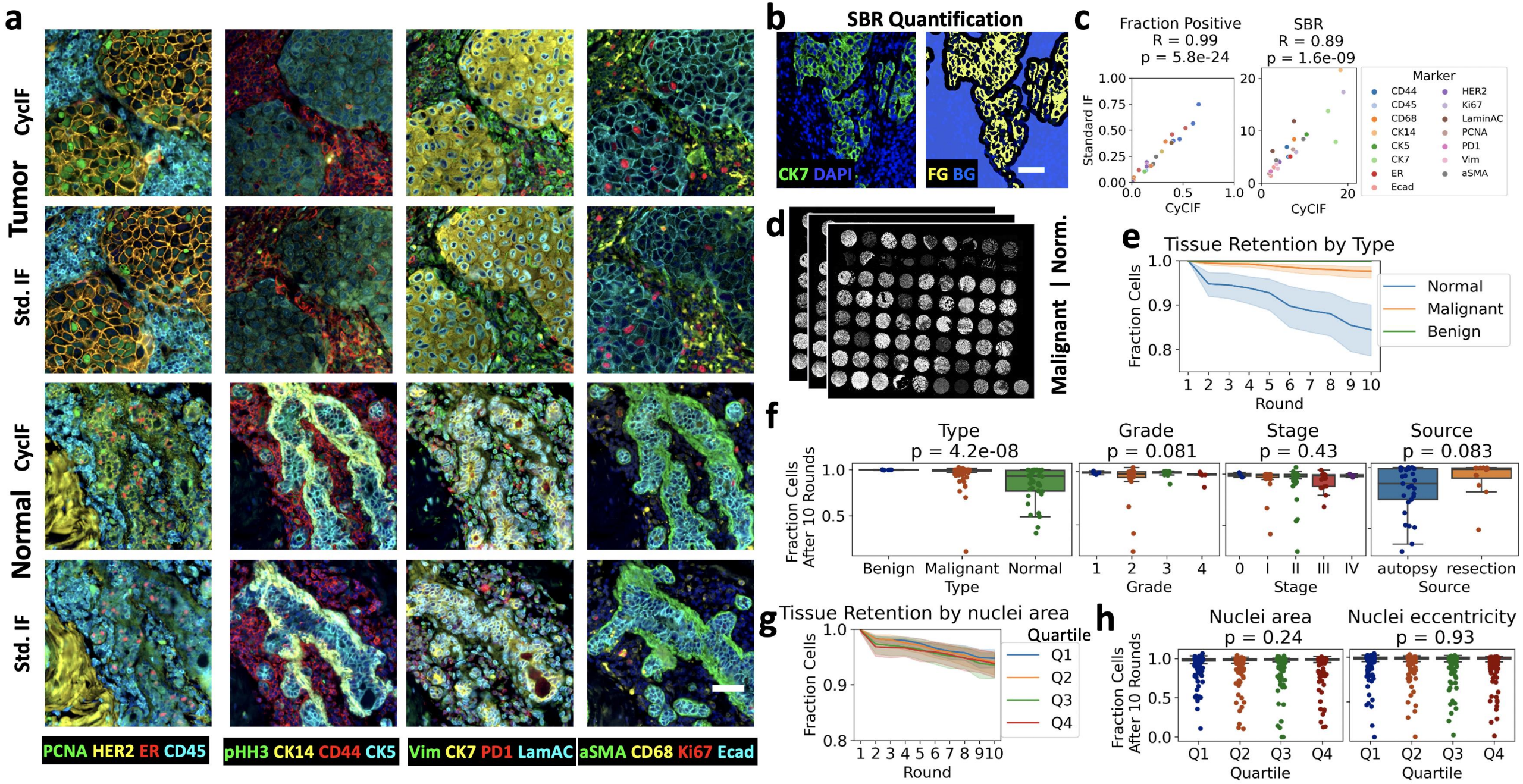
a
Tumor
CycIF
Std. IF
Normal
CycIF
Std. IF
PCNA HER2 ER CD45
pHH3 CK14 CD44 CK5
Vim CK7 PD1 LamAC
aSMA CD68 Ki67 Ecad
b
SBR Quantification
CK7 DAPI
FG BG
c
Fraction Positive
R = 0.99
p = 5.8e-24
SBR
R = 0.89
p = 1.6e-09
Standard IF
CyCIF
Marker
CD44
CD45
CD68
CK14
CK5
CK7
ER
Ecad
HER2
Ki67
LaminAC
PCNA
PD1
Vim
aSMA
d
Malignant | Norm.
e
Tissue Retention by Type
Fraction Cells
Round
Normal
Malignant
Benign
f
Type
p = 4.2e-08
Grade
p = 0.081
Stage
p = 0.43
Source
p = 0.083
Fraction Cells After 10 Rounds
Benign Malignant Normal
Type
1 2 3 4
Grade
0 I II III IV
Stage
autopsy resection
Source
g
Tissue Retention by nuclei area
Fraction Cells
Round
Quartile
Q1
Q2
Q3
Q4
h
Nuclei area
p = 0.24
Nuclei eccentricity
p = 0.93
Fraction Cells After 10 Rounds
Q1 Q2 Q3 Q4
Quartile

Fig. 2

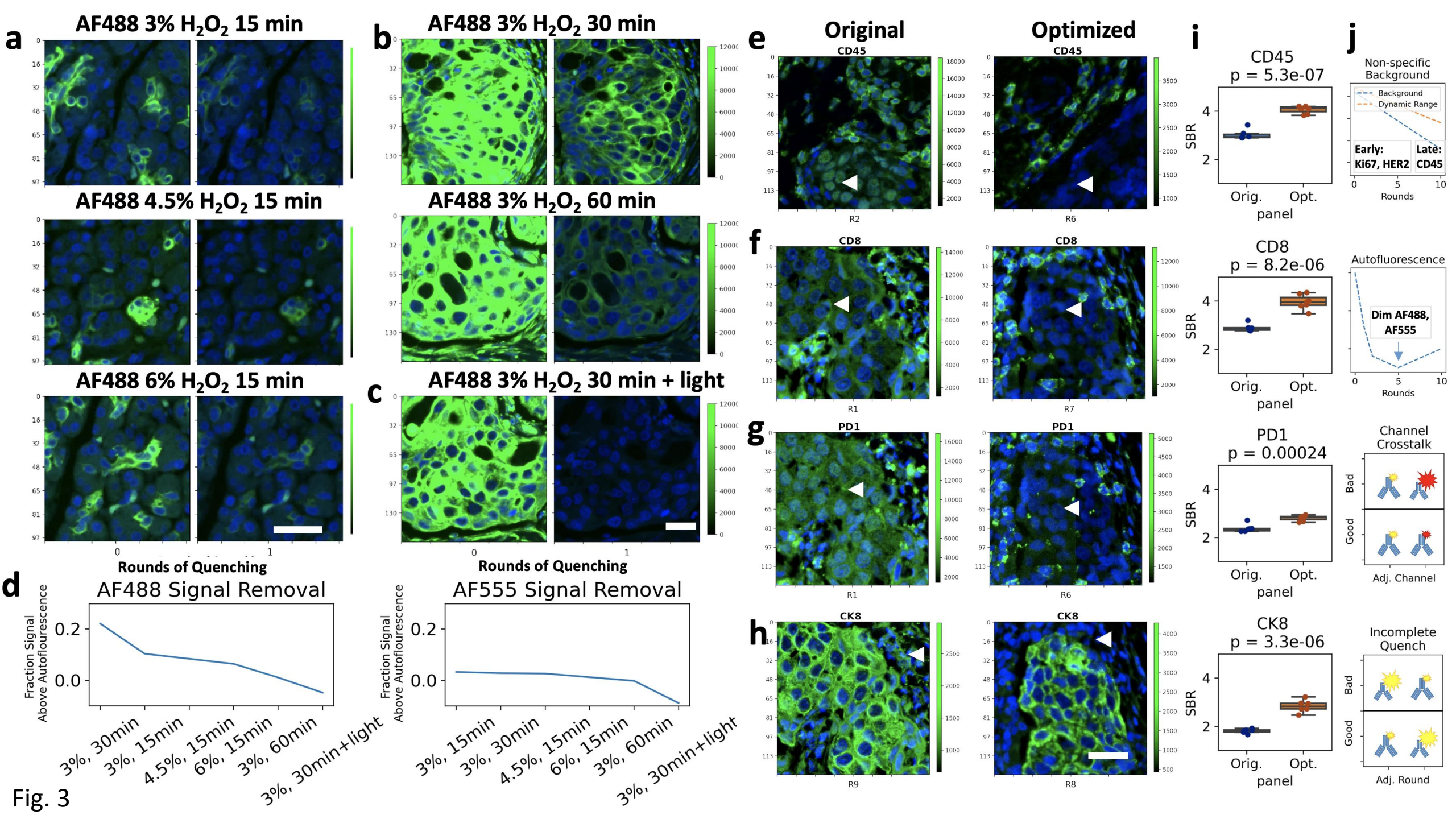
a
AF488 3% H_2O_2 15 min
AF488 4.5% H_2O_2 15 min
AF488 6% H_2O_2 15 min
b
AF488 3% H_2O_2 30 min
AF488 3% H_2O_2 60 min
c
AF488 3% H_2O_2 30 min + light
Rounds of Quenching
d
AF488 Signal Removal
AF555 Signal Removal
Fraction Signal Above Autoflourescence
3%, 30min
3%, 15min
4.5%, 15min
6%, 15min
3%, 60min
3%, 30min+light
e
Original
Optimized
CD45
R2
R6
f
CD8
R1
R7
g
PD1
R1
R6
h
CK8
R9
R8
i
CD45
p = 5.3e-07
CD8
p = 8.2e-06
PD1
p = 0.00024
CK8
p = 3.3e-06
SBR
Orig.
Opt.
panel
j
Non-specific Background
Background
Dynamic Range
Early: Ki67, HER2
Late: CD45
Rounds
Autofluorescence
Dim AF488, AF555
Channel Crosstalk
Bad
Good
Adj. Channel
Incomplete Quench
Adj. Round

Fig. 3

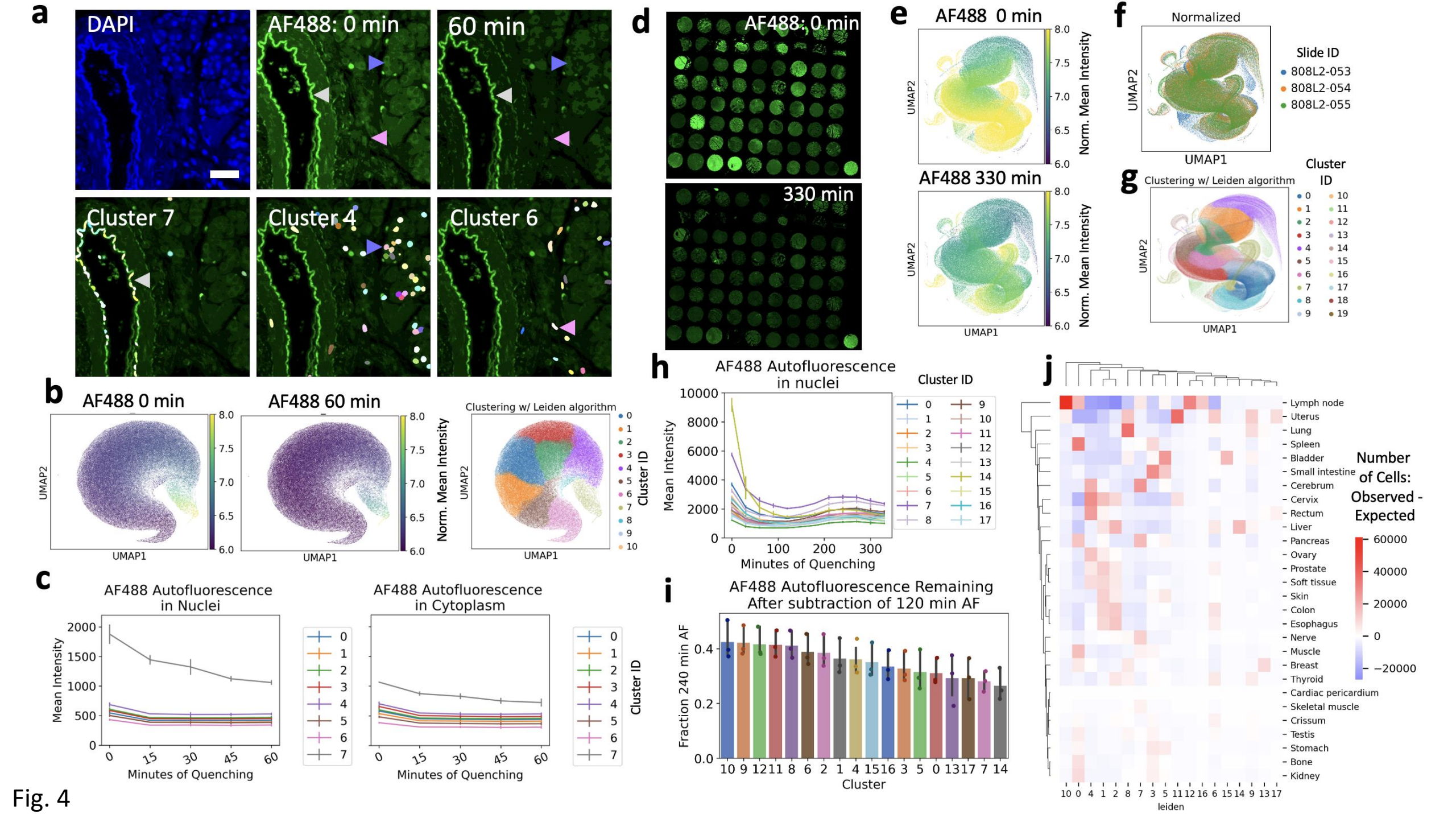
a
DAPI
AF488: 0 min
60 min
Cluster 7
Cluster 4
Cluster 6
b
AF488 0 min
AF488 60 min
Clustering w/ Leiden algorithm
UMAP1
UMAP2
Norm. Mean Intensity
Cluster ID
c
AF488 Autofluorescence in Nuclei
AF488 Autofluorescence in Cytoplasm
Mean Intensity
Minutes of Quenching
Cluster ID
d
AF488: 0 min
330 min
e
AF488 0 min
AF488 330 min
Norm. Mean Intensity
f
Normalized
Slide ID
808L2-053
808L2-054
808L2-055
g
Clustering w/ Leiden algorithm
Cluster ID
h
AF488 Autofluorescence in nuclei
Mean Intensity
Minutes of Quenching
Cluster ID
i
AF488 Autofluorescence Remaining After subtraction of 120 min AF
Fraction 240 min AF
Cluster
j
Lymph node
Uterus
Lung
Spleen
Bladder
Small intestine
Cerebrum
Cervix
Rectum
Liver
Pancreas
Ovary
Prostate
Soft tissue
Skin
Colon
Esophagus
Nerve
Muscle
Breast
Thyroid
Cardiac pericardium
Skeletal muscle
Crissum
Testis
Stomach
Bone
Kidney
leiden
Number of Cells: Observed - Expected

Fig. 4

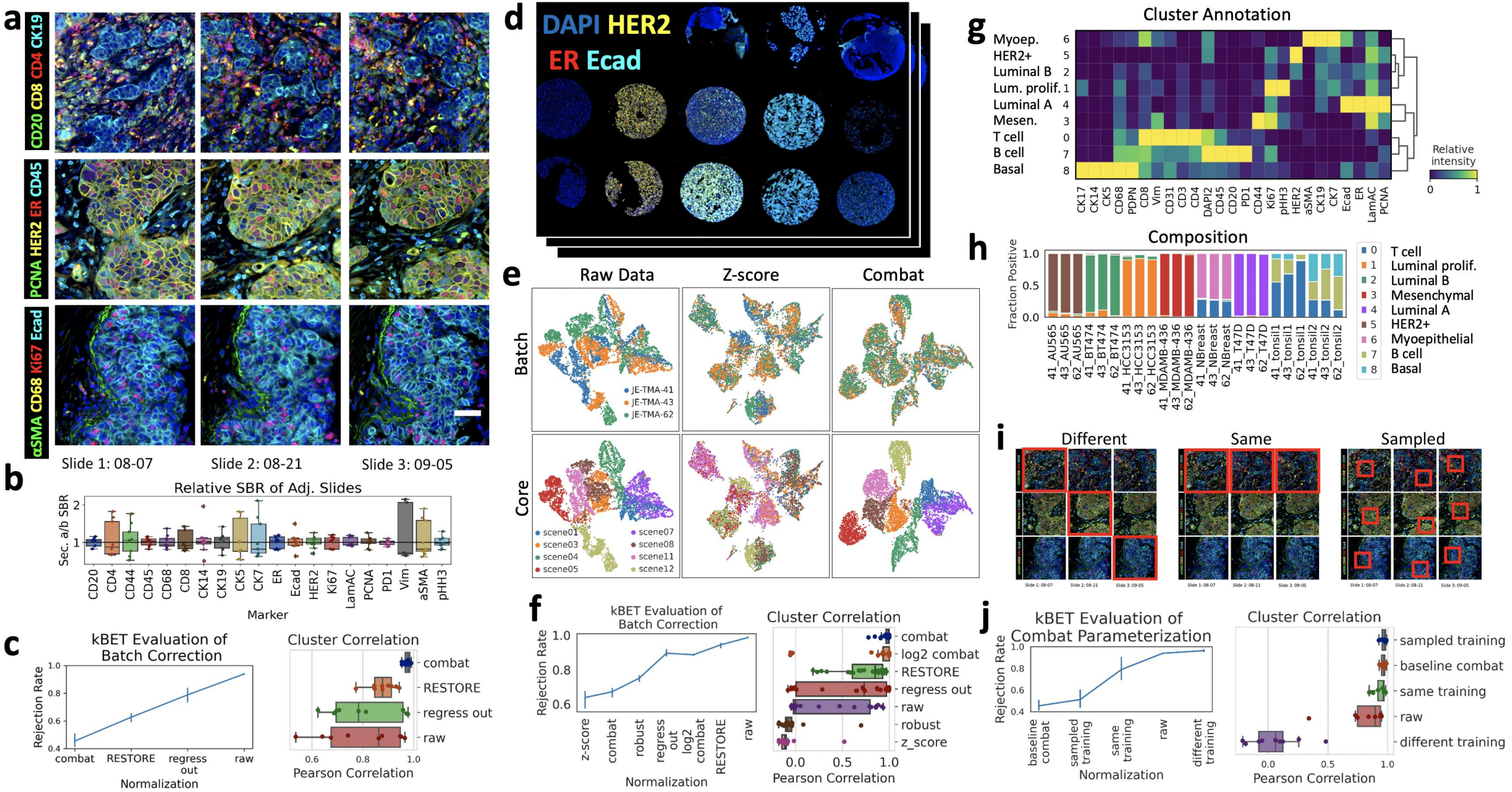
a
CD20 CD8 CD4 CK19
PCNA HER2 ER CD45
αSMA CD68 Ki67 Ecad
Slide 1: 08-07
Slide 2: 08-21
Slide 3: 09-05
b
Relative SBR of Adj. Slides
Sec. a/b SBR
CD20 CD4 CD44 CD45 CD68 CD8 CK14 CK19 CK5 CK7 ER Ecad HER2 Ki67 LamAC PCNA PD1 Vim aSMA pHH3
Marker
c
kBET Evaluation of Batch Correction
Rejection Rate
combat RESTORE regress out raw
Normalization
Cluster Correlation
combat
RESTORE
regress out
raw
Pearson Correlation
d
DAPI HER2
ER Ecad
e
Raw Data
Z-score
Combat
Batch
JE-TMA-41
JE-TMA-43
JE-TMA-62
Core
scene01
scene03
scene04
scene05
scene07
scene08
scene11
scene12
f
kBET Evaluation of Batch Correction
Rejection Rate
z-score combat robust regress out log2 combat RESTORE raw
Normalization
Cluster Correlation
combat
log2 combat
RESTORE
regress out
raw
robust
z_score
Pearson Correlation
g
Cluster Annotation
Myoep. 6
HER2+ 5
Luminal B 2
Lum. prolif. 1
Luminal A 4
Mesen. 3
T cell 0
B cell 7
Basal 8
CK17 CK14 CK5 CD68 PDPN CD8 Vim CD31 CD3 CD4 DAPI2 CD45 CD20 PD1 CD44 Ki67 pHH3 HER2 aSMA CK19 CK7 Ecad ER LamAC PCNA
Relative intensity
h
Composition
Fraction Positive
41_AU565 43_AU565 62_AU565 41_BT474 43_BT474 62_BT474 41_HCC3153 43_HCC3153 62_HCC3153 41_MDAMB-436 43_MDAMB-436 62_MDAMB-436 41_NBreast 43_NBreast 62_NBreast 41_T47D 43_T47D 62_T47D 41_tonsil1 43_tonsil1 62_tonsil1 41_tonsil2 43_tonsil2 62_tonsil2
0 T cell
1 Luminal prolif.
2 Luminal B
3 Mesenchymal
4 Luminal A
5 HER2+
6 Myoepithelial
7 B cell
8 Basal
i
Different
Same
Sampled
j
kBET Evaluation of Combat Parameterization
Rejection Rate
baseline combat
sampled training
same training
raw
different training
Normalization
Cluster Correlation
sampled training
baseline combat
same training
raw
different training
Pearson Correlation

Fig. 5